PHYSICAL REVIEW B **92**, 235138 (2015)

Experimental observation of incoherent-coherent crossover and orbital-dependent band renormalization in iron chalcogenide superconductors

Z. K. Liu,[1,2] M. Yi,[1,2] Y. Zhang,[1,3] J. Hu,[4] R. Yu,[5,6] J.-X. Zhu,[7] R.-H. He,[8] Y. L. Chen,[9] M. Hashimoto,[10] R. G. Moore,[1]
S.-K. Mo,[3] Z. Hussain,[3] Q. Si,[6] Z. Q. Mao,[4] D. H. Lu,[10] and Z.-X. Shen[1,2,*]
[1]*Stanford Institute for Materials and Energy Sciences, SLAC National Accelerator Laboratory, 2575 Sand Hill Road, Menlo Park, California 94025, USA*
[2]*Geballe Laboratory for Advanced Materials, Departments of Physics and Applied Physics, Stanford University, Stanford, California 94305, USA*
[3]*Advanced Light Source, Lawrence Berkeley National Laboratory, Berkeley, California 94720, USA*
[4]*Department of Physics and Engineering Physics, Tulane University, New Orleans, Louisiana 70118, USA*
[5]*Department of Physics, Renmin University of China, Beijing 100872, China*
[6]*Department of Physics and Astronomy, Rice University, Houston, Texas 77005, USA*
[7]*Theoretical Division, Los Alamos National Laboratory, Los Alamos, New Mexico 87545, USA*
[8]*Department of Physics, Boston College, Higgins Hall 330N, Chestnut Hill, Massachusetts 02467, USA*
[9]*Physics Department, Clarendon Laboratory, University of Oxford, Parks Road, Oxford OX1 3PU, United Kingdom*
[10]*Stanford Synchrotron Radiation Lightsource, SLAC National Accelerator Laboratory, 2575 Sand Hill Road, Menlo Park, California 94025, USA*

(Received 20 January 2015; revised manuscript received 26 November 2015; published 22 December 2015)

The level of electronic correlation has been one of the key questions in understanding the nature of superconductivity. Among the iron-based superconductors, the iron chalcogenide family exhibits the strongest electron correlations. To gauge the correlation strength, we performed a systematic angle-resolved photoemission spectroscopy study on the iron chalcogenide series $\mathrm{Fe}_{1+y}\mathrm{Se}_x\mathrm{Te}_{1-x}$ ($0 < x < 0.59$), a model system with the simplest structure. Our measurement reveals an incoherent-to-coherent crossover in the electronic structure as the selenium ratio increases and the system evolves from a weakly localized to a more itinerant state. Furthermore, we found that the effective mass of bands dominated by the d_{xy} orbital character significantly decreases with increasing selenium ratio, as compared to the d_{xz}/d_{yz} orbital-dominated bands. The orbital-dependent change in the correlation level agrees with theoretical calculations on the band structure renormalization, and may help to understand the onset of superconductivity in $\mathrm{Fe}_{1+y}\mathrm{Se}_x\mathrm{Te}_{1-x}$.

DOI: 10.1103/PhysRevB.92.235138 PACS number(s): 74.70.Xa, 71.27.+a, 79.60.−i, 74.25.Jb

I. INTRODUCTION

The nature and role of the many-body interaction have been crucial yet unsettled questions in the recently discovered iron-based superconductivity [1–3]. Among all the iron-based superconductors, the correlation level in the iron chalcogenide $\mathrm{Fe}_{1+y}\mathrm{Se}_x\mathrm{Te}_{1-x}$ (11 system) has been predicted to be one of the strongest [3–5], which is confirmed by transport [6,7], neutron scattering [8], optical spectroscopy [9], and photoemission spectroscopy [10–12] experiments. The mechanism for strong correlation in the parent compound of the 11 system, $\mathrm{Fe}_{1.02}\mathrm{Te}$, was addressed in our previous angle-resolved photoemission spectroscopy (ARPES) study: The electronic structure in the antiferromagnetic (AFM) phase is featured by the characteristic "peak-dip-hump" features and quasiparticle dispersion with huge band renormalization (∼90), which we attribute to coherent polarons formed by the interplay of a large magnetic moment and electron-phonon coupling [13]. The coherent polaronic behavior naturally explains the metallicity in the AFM state of $\mathrm{Fe}_{1.02}\mathrm{Te}$. However, we are still lacking a systematic study on the evolution of the correlation strength with the change of selenium ratio from the metallic AFM phase ($x < 0.1$) to the weakly localized phase ($0.1 < x < 0.28$) and finally the superconducting/metallic phase ($x > 0.28$) [6] [Fig. 1(a)], where the correlation level is described by a large band renormalization, reported to be 6–20 for optimally doped $\mathrm{FeSe}_{0.45}\mathrm{Te}_{0.55}$ ($T_c = 14.5$ K) [10].

In this paper, we present a systematic study of the electron correlation effect using ARPES on a series of $\mathrm{Fe}_{1+y}\mathrm{Se}_x\mathrm{Te}_{1-x}$ samples with increasing selenium ratios ($y < 0.02$, $x = 0$, 0.11, 0.2, 0.25, 0.28, 0.35, 0.44, 0.59). Our results show that the electronic structure of the $s = 0.11$ sample in the weakly localized phase is similar to that of $\mathrm{Fe}_{1.02}\mathrm{Te}$ ($x = 0$ sample) above the AFM transition temperature (T_N). With a higher selenium ratio, the spectral weight of the coherent quasiparticles becomes increasingly pronounced, indicating an incoherent-to-coherent crossover in the electronic structure. Furthermore, we find that the effective mass renormalization of the bands dominated by the d_{xy} orbital character decreases with selenium substitution, while that with the d_{xz}/d_{yz} character does not show much of a change. Our results reveal an orbital-dependent decrease of electronic correlations as superconductivity emerges in the iron chalcogenide $\mathrm{Fe}_{1+y}\mathrm{Se}_x\mathrm{Te}_{1-x}$. Such an evolution of the orbital-dependent electronic correlation effect is observed so far only in iron chalcogenides, making them a unique family to study the interplay between strong correlations, multiorbital physics, and superconductivity in iron-based superconductors.

II. EXPERIMENTAL RESULTS

High-quality $\mathrm{Fe}_{1+y}\mathrm{Se}_x\mathrm{Te}_{1-x}$ single crystals were synthesized using the flux method [15]. The excess Fe ratio was kept

---

[*] zxshen@stanford.edu

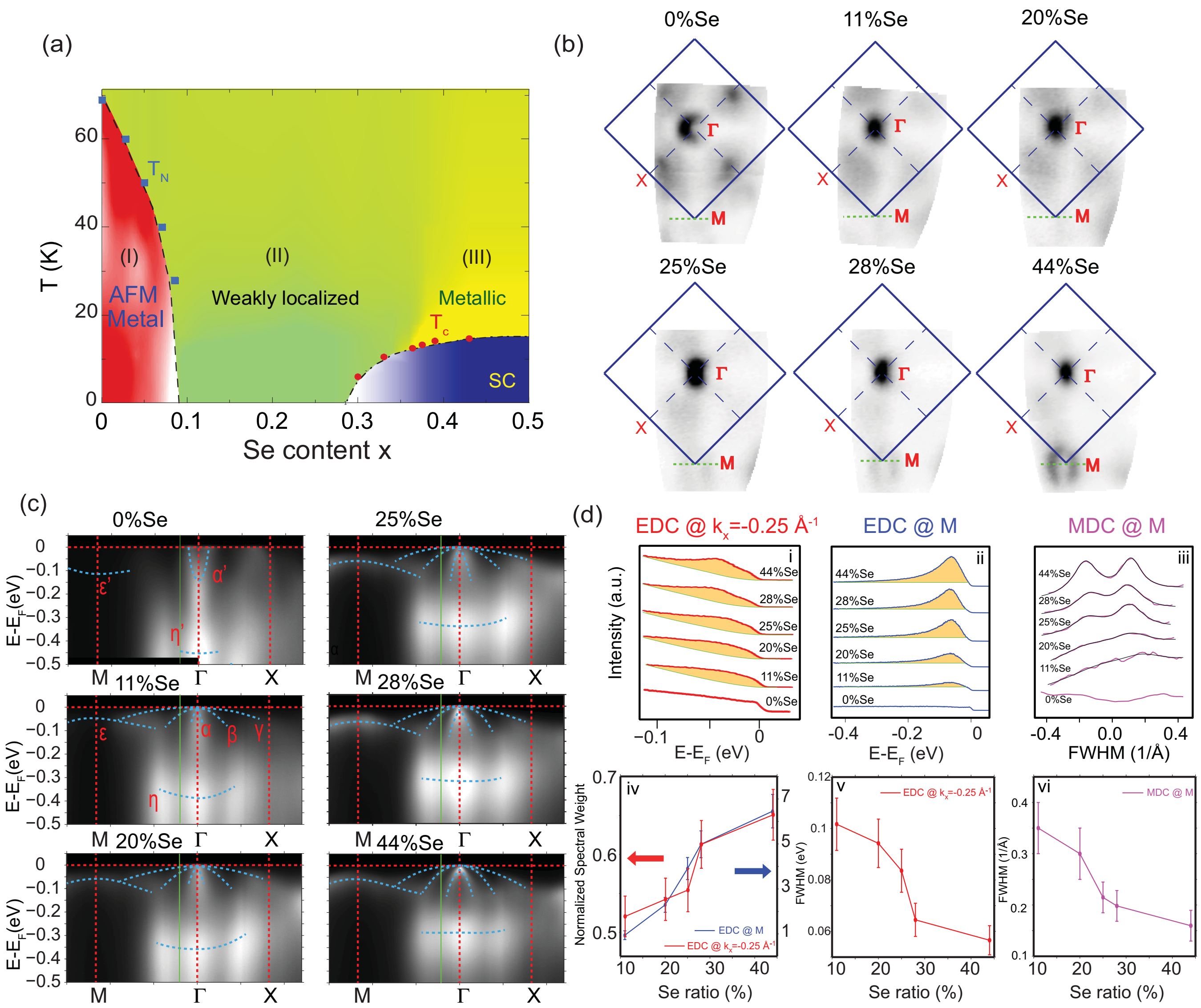

FIG. 1. (Color online) (a) Phase diagram of $\mathrm{Fe}_{1+y}\mathrm{Se}_x\mathrm{Te}_{1-x}$ adapted from Ref. [14]. T_N and T_c represent the Néel temperature and onset superconducting transition temperature probed by specific heat, neutron scattering, and magnetic susceptibility measurements. (b) Fermi surface map of $\mathrm{Fe}_{1+y}\mathrm{Se}_x\mathrm{Te}_{1-x}$ with various x measured with 22 eV excitation energy at $T = 10$ K. The photoemission intensity is integrated within a 20 meV window around the Fermi level. The dashed green lines indicate the positions of MDCs plotted in (d)(iii). (c) Photoemission intensity of the cut along the M-Γ-X direction. The dotted curves are guides to the eyes of different band dispersions. The green lines indicate the positions of EDCs plotted in (d)(i). (d)(i) EDCs at $k_x = -0.25$ Å^{-1} from $\mathrm{Fe}_{1+y}\mathrm{Se}_x\mathrm{Te}_{1-x}$ with different x. EDCs from $x = 11\%$ to 44% are fitted to a Shirley background (green curve) and a Lorentzian for the β band (orange), convolved by the Fermi-Dirac function. (ii) EDCs at M from $\mathrm{Fe}_{1+y}\mathrm{Se}_x\mathrm{Te}_{1-x}$ with different x. EDCs from $x = 11\%$ to 44% are fitted by a constant background (green curve) and a Lorentzian for the ε/ε' band (orange), convolved by the Fermi-Dirac function. (iii) MDCs on E_F across M [directions shown in (b)] from $\mathrm{Fe}_{1+y}\mathrm{Se}_x\mathrm{Te}_{1-x}$ with different x. For MDCs from $x = 11\%$ to 44%, two Lorentzians plus linear background fitting curves are overlapped with the plot (black curves). (iv) Normalized spectral weight of the fitted quasiparticle peak from (i) (red markers) and (ii) (blue markers) plotted against the Se ratio. (v) EDC width of the fitted quasiparticle peak from (i) plotted against the Se ratio. (vi) MDC width of the fitted peak from (iii) plotted against the Se ratio.

as low as possible and was determined by energy-dispersive x-ray spectrometry to be around 2%. ARPES measurements were performed at beamline 5-4 at Stanford Synchrotron Radiation Lightsource (SSRL) (photon energy $h\nu = 22$–26 eV) and beamline 10.0.1 at Advanced Light Source (ALS), LBNL (photon energy $h\nu = 50$ eV). The samples were cleaved *in situ*, and measured in ultrahigh vacuum with a base pressure of better than 3×10^{-11} Torr, and data were recorded by a Scienta R4000 analyzer at a 10 K sample temperature. The energy (angular) resolution was 8 meV (0.2°, i.e., ~0.008 Å^{-1} for photoelectrons generated by 22–26 eV photons) for the SSRL setup, and 15 meV (0.2°, i.e., 0.012 Å^{-1} for photoelectrons generated by 50 eV photons) for the ALS setup.

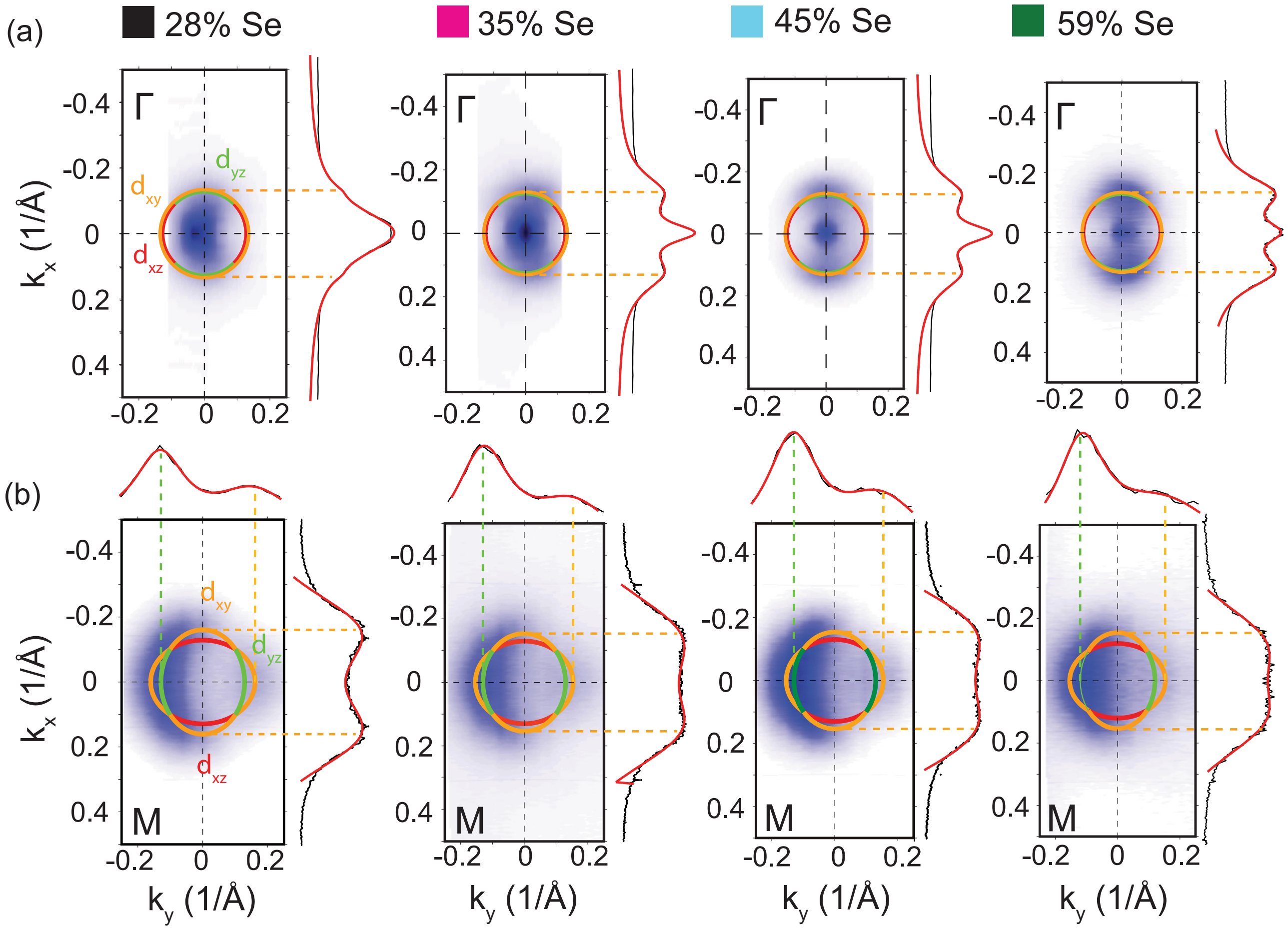

FIG. 2. (Color online) (a) Fermi surface maps of features around the Γ point from $Fe_{1+y}Se_xTe_{1-x}$ with various x measured with 22 eV excitation energy at $T = 10$ K. A schematic of the FSs is plotted on top of the map with different colors representing bands with different orbital characters. The momentum distribution curve (black curve) along $k_y = 0$ is plotted on the right side of each figure, together with the three-Lorentzian fitting curve (red curve) showing the actual positions of the Fermi surface crossing (k_F). (b) Fermi surface map of features around the M point from $Fe_{1+y}Se_xTe_{1-x}$ with various x measured with 26 eV excitation energy at $T = 10$ K. A schematic of the Fermi surface is plotted on top of the map with different colors representing bands with different orbital characters. The momentum distribution curve (black curve) along $k_y(k_x) = 0$ is plotted on the right (top) side of each figure, together with the two-Lorentzian (Lorentzian+Gaussian) fitting curve (red curve) showing the actual positions of the Fermi surface crossing (k_F).

A. Incoherent-coherent crossover

The measured Fermi surfaces (FSs) and band dispersions along the high symmetry M-Γ-X directions [the high symmetry points are defined in the Brillouin zone in the reciprocal space of 2-Fe unit cell as shown in Fig. 1(b)] for samples with selenium ratios between 0 and 0.44 are plotted in Figs. 1(b) and 1(c), respectively. First, the electronic structures of $x = 0$ and 0.11 at low temperatures are drastically different. $Fe_{1.02}Te$ in the AFM phase is characterized by an electron pocket at Γ, a finite spectral intensity around X, and almost no intensity at M (see Ref. [13] for details). At a selenium ratio of 0.11 where the system is in the weakly localized state, the electronlike pocket at Γ becomes holelike, producing a peanutlike shape on the FS. Bands at M start to be noticeable while the spectral weight around the X point weakens. Notably, such a doping evolution in the electronic structure is very similar to that of the temperature-induced change in $Fe_{1.02}Te$ from below to above the AFM transition temperature T_N [13], that hence could be understood as the result of an electronic band reconstruction across the AFM phase transition.

When the selenium ratio increases from 0.11 to 0.44, the changes in the electronic band structure become more gradual. From the FS mapping [Fig. 1(b)], we see that the feature at M becomes stronger in intensity with a gradual emergence of electronlike pockets, while the intensity at X fades out. Such a FS evolution may be closely related to the suppression of the $(\pi,0)$ short-range magnetic order and the enhancement of the (π,π) magnetic fluctuation with selenium substitution, as reported in the neutron scattering experiments in the weakly localized phase of $Fe_{1+y}Se_xTe_{1-x}$ [6,16]. At the same time, the band dispersions do not have drastic changes in energy, except for the electronlike band around ~400 meV below E_F at Γ [labeled as the η band in Fig. 1(c) with dominantly d_{z^2} orbital character], which shifts systematically from −400 to −300 meV. This band shift is well captured by the density functional calculation results [17].

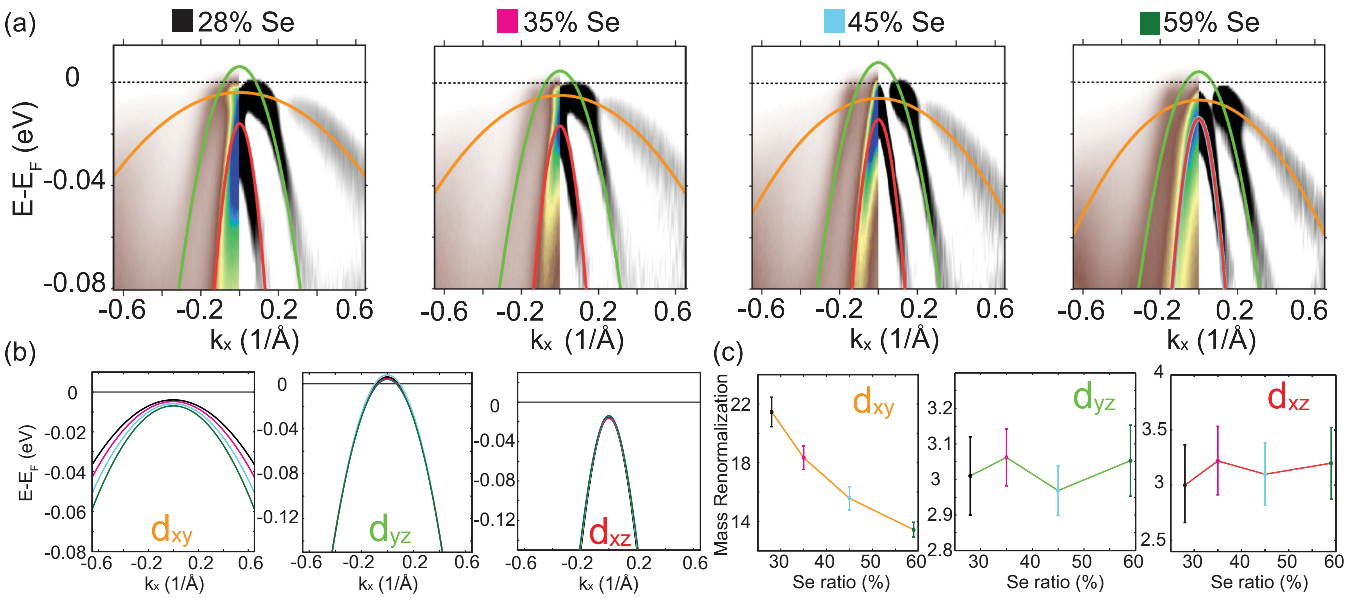

FIG. 3. (Color online) (a) Photoemission intensity of the cut around Γ along the Γ-*M* direction for $Fe_{1+y}Se_xTe_{1-x}$ with various x. The original data are plotted on the left side of the each panel while the second derivatives of the same data are plotted on the right side for better visualization of each band. The extracted dispersion for each band is plotted on top of each image plot with different colors representing different dominating orbital characters. (b) Stack plot of fitted band dispersions. Bands with different orbitals are plotted in different panels. In each panel different colors represent samples with different x. (c) Plot of the extracted effective band mass renormalization factor vs the selenium ratio. Band masses with different orbitals are plotted in different panels.

A more significant change occurs in the evolution of the spectral weight and linewidth. As the selenium ratio increases, we found that, in the high symmetry cuts [Fig. 1(c)], the broad and smeared dispersions become narrower and sharper, indicating that the spectral weight of the coherent quasiparticles becomes stronger over the incoherent background, as is clearly shown by the energy distribution curve (EDC) evolution of the β band around Γ [Fig. 1(d)(i)] and the ϵ band around M [Fig. 1(d)(ii)], and also the momentum distribution curve (MDC) evolution on E_F across the M point [Fig. 1(d)(iii)]. The increase of the spectral weight [Fig. 1(d)(iv)] and decrease of the linewidth [Fig. 1(d)(v)(vi)] of the coherent quasiparticles are very similar to ARPES observations of the doping dependence of other strongly correlated materials (e.g., cuprates [18,19]); it is a direct manifestation of the incoherent-to-coherent crossover behavior of the electrons, concomitant with $Fe_{1+y}Se_xTe_{1-x}$ evolving from the weakly localized phase to the metallic phase when the selenium ratio increases from 0.11 to 0.44. From 0.44 to 0.59, our measured quasiparticle spectral weights are fluctuating due to sample quality variations rather than showing the systematic trends of evolution.

B. Orbital-dependent band renormalization

Such an increase in coherence could not be interpreted as the effect of impurity scattering since the level of disorder actually increases with selenium substitution in $Fe_{1+y}Te$ and maximizes at $Fe_{1+y}Se_{0.5}Te_{0.5}$ [20]. Rather, the crossover behavior strongly suggests the change in the electronic correlation strength. To address this problem, we performed a detailed analysis on the electronic structure evolution of samples with selenium ratios from $x = 0.28$ to 0.59 (the spectral weight of the dispersions for $x < 0.28$ is too small, making such an analysis difficult). Figure 2 plots the measured FSs at both the Γ [Fig. 2(a)] and M [Fig. 2(b)] points. At the Γ point, we find the "peanut shape" in the FS is part of a circular hole pocket with a mixed orbital content of d_{xy} and d_{xz}/d_{yz} due to band hybridization (see the Supplemental Material, Part II [21]). The reason we did not observe a full circle is due to the suppression from the matrix element (see the Supplemental Material, Part I [21]). The intensity at exact Γ comes from the band top of the inner d_{xz}/d_{yz} band. At the M point, we observe two intersecting ellipses, with different segments coming from different orbitals. Some parts of the two ellipses are not visible in the data due to the suppression from the matrix element. To determine the Fermi pocket size, we find the maximum and minimum openings of the pockets from fitting the contour plots. The schematics of the FSs can then be drawn by considering the fourfold crystal symmetry of the tetragonal state. The carrier concentration level can then be evaluated by counting the Fermi surface volume. The calculated net doping level is 0.003–0.012 electron/Fe, indicating that the 11 system is almost electron-hole balanced with the additional electrons perhaps coming from the excessive interstitial Fe atoms [15]. Furthermore, we do not observe any obvious change in either the electron or hole pockets for samples with different selenium ratios, confirming the isovalent nature of the selenium/tellurium substitution.

The electronic band dispersions near the Fermi level do not shift noticeably in position but exhibit a systematic change in curvature. We extracted the dispersions by locating the peak positions from both the energy and momentum distribution curves. Around the Γ point we could identify three different hole bands which are dominated by different orbital characters (see the Supplemental Material, Part I [21]). By fitting each of the dispersions to a parabolic curve, we can extract the effective mass of each band [Figs. 3(a) and 3(b)]. As Fig. 3(c) shows, the d_{xy} band has the largest effective mass renormalization compared with the density functional calculation [17], while the other bands have much smaller renormalization factors ($\sim$3 for the d_{yz} and the d_{xz} bands). Moreover, only the renormalization factor of the d_{xy} band shows a significant doping dependence, decreasing from 22 to 14 as the selenium ratio increases from 0.28 to 0.59. For the d_{xz}/d_{yz} bands, the extracted effective masses do not change noticeably over this doping range.

We applied the same analysis to the electron pockets at M and observed a similar behavior (see the Supplemental Material, Part III [21]). All together, we have found that bands dominated by the d_{xy} orbital character have a much larger renormalization compared to bands of other orbitals, and the renormalization monotonically reduces as the selenium ratio increases while the other orbitals do not have such an effect. Therefore, by using an effective band mass as the correlation level indicator, we have discovered there is a reduction in (a yet still strong) correlation as selenium replaces tellurium in $Fe_{1+y}Se_xTe_{1-x}$, and this correlation reduction has the most significant effect in bands with the d_{xy} orbital character.

III. THEORETICAL INTERPRETATION

Compared to the band renormalization change that happens to all the t_{2g} bands in Co-doped $BaFe_2As_2$ systems [22], such an orbital-dependent renormalization evolution is a unique feature for the 11 system. So far, there have been several theoretical works discussing the level of correlation and unique orbital-dependent physics in the 11 system. In a theoretical study based on the dynamical mean-field theory, Ref. [3] has pointed out that the correlation effects in Fe pnictides/chalcogenides come from the Hund's coupling and that the structural parameters have a strong impact on the overall correlation strength and orbital selectivity. The longer Fe-chalcogen bond length compared to that of Fe-pnictigen would result in more localized electrons. Meanwhile, the Ch-Fe-Ch bond angle, which controls crystal field splitting, is much smaller from that of an ideal tetrahedron in iron chalcogenides. As a result, electrons in the in-plane d_{xy} orbitals are more localized in iron chalcogenides compared to other orbitals. Given the structural sensitivity, the substitution of smaller selenium atoms for bigger tellurium atoms would modify the structural parameters and decrease the correlation

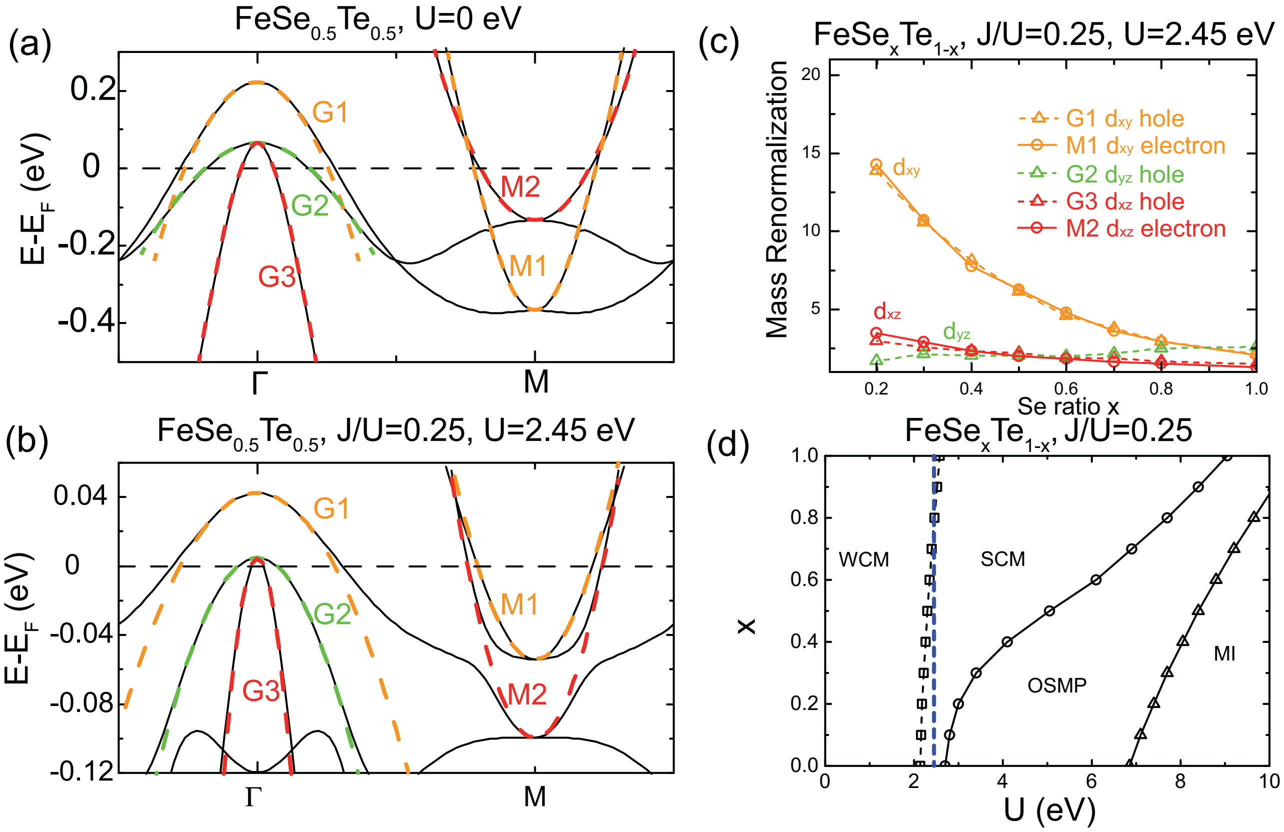

FIG. 4. (Color online) (a), (b) Band structure calculation results on $FeSe_{0.5}Te_{0.5}$ with Coulomb repulsion $U = 0$ and Hund's coupling $J = 0$ for (a) and $U = 2.45$ eV, $J/U = 0.25$ for (b). G1–G3 labels the three hole bands and M1–M2 labels the two electron bands. The dotted color curves indicate the extraction of the effective mass of different orbitals by parabolic curve fittings to portions of dispersion near the band top (bottom). Orange, green, and red curves represent the d_{xy}, d_{yz}, and d_{xz} orbitals. The breaking of dispersion near M is due to the band hybridization between the d_{xz} electron band and d_{xy} hole band. (c) Calculated mass renormalization for different bands from samples with different selenium ratios x in $FeSe_xTe_{1-x}$. The mass renormalization is calculated by dividing the effective mass from the calculated band structure with $U = 2.45$ eV, $J/U = 0.25$ by that from $U = J = 0$. Different marks with color indicate the renormalization of different bands, and different colors label different orbitals. (d) Calculated phase diagram of $FeSe_xTe_{1-x}$ as a function of selenium ratio x and Coulomb interaction U. The blue dotted line denotes where $U = 2.45$ eV and the calculated mass renormalization agrees best with the actual experimental results. WCM: Weakly correlated metal. SCM: Strongly correlated metal. OSMP: Orbital-selective Mott phase. MI: Mott insulator.

level and orbital selectivity. In another work based on a slave-spin mean-field method [23,24], the authors proposed that, due to the strong intraorbital Coulomb repulsion U and Hund's coupling J, the iron chalcogenide family is in proximity to an orbital-selective Mott phase (OSMP), where the d_{xy} orbital is Mott localized while the other orbitals remain itinerant. The physical scenario of OSMP has been previously proposed and discussed in $Ca_{2-x}Sr_xRuO_4$ [25–27] and iron-based superconductors [23,24,28,29].

Both works would explain our observations on the correlation level change and orbital selectivity in $FeSe_xTe_{1-x}$. As an illustration, we applied the model from Refs. [23,24] to the $FeSe_xTe_{1-x}$ family and the calculation results are summarized in Fig. 4 (details of the calculation may be found in the Supplemental Material, Part VI [21]; we also note the fact that the d_{xy} hole band is higher than the d_{yz} and d_{xz} hole bands is due to the exclusion of spin-orbit coupling in the theoretical calculation). With the inclusion of moderate U and J ($U = 2.45$ eV, $J/U = 0.25$) in the model, the dispersion of $FeSe_{0.5}Te_{0.5}$ [Fig. 4(b)] is found to be greatly renormalized compared to the $U = J = 0$ case [Fig. 4(a)]. The calculated mass renormalizations at the same value of U and J for different x values in $FeSe_xTe_{1-x}$ well reproduce the change in the overall correlation strength and orbital selectivity, as observed [Fig. 4(c)]. The agreement with the experimental result shows that $FeSe_xTe_{1-x}$ is overall in the strongly correlated metal phase and loses correlation with increasing x [Fig. 4(d)]. The calculation further proposed that the correlated metal phase is in proximity to an orbital-selective Mott phase and raising the temperature is one potential path to enter such a phase [30].

IV. DISCUSSIONS

It should be noted that our observation of the correlation evolution of $Fe_{1+y}Se_xTe_{1-x}$ has only extended to selenium ratios of up to 0.59. Single crystals with selenium ratios higher than that have been found to be hard to stabilize [31]. However, in our recent ARPES measurement, we have observed very renormalized d_{xy} hole bands with a renormalization factor ~10 for $K_xFe_{2-y}Se_2$ [29,30]. In addition, a recent ARPES report on a single crystal of FeSe found the d_{xy}, d_{yz}, and d_{xz} hole band renormalizations to be 9, 3, and 3.7, respectively, fully consistent with our observations of the trend [12]. Therefore, the large d_{xy} orbital band renormalization appears to be universal to all iron chalcogenides, making it unique among all iron-based superconductors [30].

The nature of the strong correlation may be critical to the understanding of superconductivity in iron chalcogenides. In $Fe_{1+y}Se_xTe_{1-x}$, the level of correlation seems to be the primary tuning factor for superconductivity since the doping level and the underlying Fermi surface topology do not change. For $K_xFe_{2-y}Se_2$, where T_c is comparable to iron pnictides, the lack of hole pockets makes a weak-coupling Fermi surface nesting picture unlikely. Hence, the superconducting pairing mechanism may stem from strong correlations that lead to strong local pairing. As the d_{xy} band participates in superconducting pairing and is most sensitive to the change of correlation among all Fe $3d$ bands, its band renormalization would serve as an accurate gauge for the correlation level and pairing strength.

Recently, we became aware of a similar report [32] that also addressed the evolution from incoherent to coherent electronic states in $FeSe_xTe_{1-x}$, consistent with our conclusion. In addition to Ref. [32], our discovery of orbital-dependent band renormalization provides a deeper understanding of the nature of the strong correlations in multiple orbital systems, such as $Fe_{1+y}Se_xTe_{1-x}$.

ACKNOWLEDGMENTS

ARPES experiments were performed at the Stanford Synchrotron Radiation Lightsource and the Advanced Light Source, which are both operated by the Office of Basic Energy Sciences, U.S. Department of Energy. The Stanford work is supported by the U.S. DOE, Office of Basic Energy Science, Division of Materials Science and Engineering, under Award No. DE-AC02-76SF00515. The work at Tulane is supported by the NSF under Grant No. DMR-1205469 and the LA-SiGMA program under Award No. EPS-1003897. The work at Rice has been supported by NSF Grant No. DMR-1309531 and the Robert A. Welch Foundation Grant No. C-1411. The work at Renmin University has been supported by the National Science Foundation of China Grant No. 11374361, and the Fundamental Research Funds for the Central Universities and the Research Funds of Renmin University of China.

---

[1] J. Paglione and R. L. Greene, Nat. Phys. **6**, 645 (2010).
[2] D. C. Johnston, Adv. Phys. **59**, 803 (2010).
[3] Z. P. Yin, K. Haule, and G. Kotliar, Nat. Mater. **10**, 932 (2011).
[4] M. Aichhorn, S. Biermann, T. Miyake, A. Georges, and M. Imada, Phys. Rev. B **82**, 064504 (2010).
[5] Z. P. Yin, K. Haule, and G. Kotliar, Phys. Rev. B **86**, 195141 (2012).
[6] T. J. Liu, J. Hu, B. Qian, D. Fobes, Z. Q. Mao, W. Bao, M. Reehuis, S. A. J. Kimber, K. Prokes, S. Matas, D. N. Argyriou, A. Hiess, A. Rotaru, H. Pham, L. Spinu, Y. Qiu, V. Thampy, A. T. Savici, J. A. Rodriguez, and C. Broholm, Nat. Mater. **9**, 718 (2010).
[7] T. Noji, M. Imaizumi, T. Suzuki, T. Adachi, M. Kato, and Y. Koike, J. Phys. Soc. Jpn. **81**, 054708 (2012).
[8] S. Li, C. de la Cruz, Q. Huang, Y. Chen, J. W. Lynn, J. Hu, Y.-L. Huang, F.-C. Hsu, K.-W. Yeh, M.-K. Wu, and P. Dai, Phys. Rev. B **79**, 054503 (2009).
[9] G. F. Chen, Z. G. Chen, J. Dong, W. Z. Hu, G. Li, X. D. Zhang, P. Zheng, J. L. Luo, and N. L. Wang, Phys. Rev. B **79**, 140509 (2009).
[10] A. Tamai, A. Y. Ganin, E. Rozbicki, J. Bacsa, W. Meevasana, P. D. C. King, M. Caffio, R. Schaub, S. Margadonna, K. Prassides, M. J. Rosseinsky, and F. Baumberger, Phys. Rev. Lett. **104**, 097002 (2010).

[11] A. Yamasaki, Y. Matsui, S. Imada, K. Takase, H. Azuma, T. Muro, Y. Kato, A. Higashiya, A. Sekiyama, S. Suga, M. Yabashi, K. Tamasaku, T. Ishikawa, K. Terashima, H. Kobori, A. Sugimura, N. Umeyama, H. Sato, Y. Hara, N. Miyagawa, and S. I. Ikeda, Phys. Rev. B **82**, 184511 (2010).

[12] J. Maletz, V. B. Zabolotnyy, D. V. Evtushinsky, S. Thirupathaiah, A. U. B. Wolter, L. Harnagea, A. N. Yaresko, A. N. Vasiliev, D. A. Chareev, A. E. Bohmer, F. Hardy, T. Wolf, C. Meingast, E. D. L. Rienks, B. Buchner, and S. V. Borisenko, Phys. Rev. B **89**, 220506 (2014).

[13] Z. K. Liu, R. H. He, D. H. Lu, M. Yi, Y. L. Chen, M. Hashimoto, R. G. Moore, S. K. Mo, E. A. Nowadnick, J. Hu, T. J. Liu, Z. Q. Mao, T. P. Devereaux, Z. Hussain, and Z. X. Shen, Phys. Rev. Lett. **110**, 037003 (2013).

[14] J. Hu, T. J. Liu, B. Qian, and Z. Q. Mao, Phys. Rev. B **88**, 094505 (2013).

[15] T. J. Liu, X. Ke, B. Qian, J. Hu, D. Fobes, E. K. Vehstedt, H. Pham, J. H. Yang, M. H. Fang, L. Spinu, P. Schiffer, Y. Liu, and Z. Q. Mao, Phys. Rev. B **80**, 174509 (2009).

[16] Z. Xu, J. Wen, G. Xu, Q. Jie, Z. Lin, Q. Li, S. Chi, D. K. Singh, G. Gu, and J. M. Tranquada, Phys. Rev. B **82**, 104525 (2010).

[17] A. Subedi, L. Zhang, D. J. Singh, and M. H. Du, Phys. Rev. B **78**, 134514 (2008).

[18] K. M. Shen, F. Ronning, D. H. Lu, W. S. Lee, N. J. C. Ingle, W. Meevasana, F. Baumberger, A. Damascelli, N. P. Armitage, L. L. Miller, Y. Kohsaka, M. Azuma, M. Takano, H. Takagi, and Z. X. Shen, Phys. Rev. Lett. **93**, 267002 (2004).

[19] N. P. Armitage, F. Ronning, D. H. Lu, C. Kim, A. Damascelli, K. M. Shen, D. L. Feng, H. Eisaki, Z. X. Shen, P. K. Mang, N. Kaneko, M. Greven, Y. Onose, Y. Taguchi, and Y. Tokura, Phys. Rev. Lett. **88**, 257001 (2002).

[20] S. V. Rajasekaran, T. Tite, Y. M. Chang, R. Sankar, and F. C. Chou, J. Mater. Sci. **46**, 7582 (2011).

[21] See Supplemental Material at http://link.aps.org/supplemental/10.1103/PhysRevB.92.235138 for further discussion on the bandstructure of $\mathrm{Fe_{1+y}Se_xTe_{1-x}}$.

[22] T. Sudayama, Y. Wakisaka, T. Mizokawa, S. Ibuka, R. Morinaga, T. J. Sato, M. Arita, H. Namatame, M. Taniguchi, and N. L. Saini, J. Phys. Soc. Jpn. **80**, 113707 (2011).

[23] R. Yu and Q. Si, Phys. Rev. Lett. **110**, 146402 (2013).

[24] R. Yu and Q. Si, Phys. Rev. B **84**, 235115 (2011).

[25] V. I. Anisimov, I. A. Nekrasov, D. E. Kondakov, T. M. Rice, and M. Sigrist, Eur. Phys. J. B **25**, 191 (2002).

[26] A. Koga, N. Kawakami, T. M. Rice, and M. Sigrist, Phys. Rev. Lett. **92**, 216402 (2004).

[27] L. de' Medici, A. Georges, and S. Biermann, Phys. Rev. B **72**, 205124 (2005).

[28] L. de' Medici, S. R. Hassan, M. Capone, and X. Dai, Phys. Rev. Lett. **102**, 126401 (2009).

[29] M. Yi, D. H. Lu, R. Yu, S. C. Riggs, J. H. Chu, B. Lv, Z. K. Liu, M. Lu, Y. T. Cui, M. Hashimoto, S. K. Mo, Z. Hussain, C. W. Chu, I. R. Fisher, Q. Si, and Z. X. Shen, Phys. Rev. Lett. **110**, 067003 (2013).

[30] M. Yi, Z. K. Liu, Y. Zhang, R. Yu, J. X. Zhu, J. J. Lee, R. G. Moore, F. T. Schmitt, W. Li, S. C. Riggs, J. H. Chu, B. Lv, J. Hu, M. Hashimoto, S. K. Mo, Z. Hussain, Z. Q. Mao, C. W. Chu, I. R. Fisher, Q. Si, Z. X. Shen, and D. H. Lu, Nat. Commun. **6**, 7777 (2015).

[31] Y. Mizuguchi and Y. Takano, J. Phys. Soc. Jpn. **79**, 102001 (2010).

[32] E. Ieki, K. Nakayama, Y. Miyata, T. Sato, H. Miao, N. Xu, X. P. Wang, P. Zhang, T. Qian, P. Richard, Z. J. Xu, J. S. Wen, G. D. Gu, H. Q. Luo, H. H. Wen, H. Ding, and T. Takahashi, Phys. Rev. B **89**, 140506 (2014).